Article

Experimental Investigation of the Leaf Type Bearing Structure with Undersprings Under Dynamic Excitation

Hannes Schmiedeke [1,*], Michael Sinapius [1] and Nontavut Prechavut [2]

[1] Institute of Mechanics and Adaptronics, TU Braunschweig, 38106 Braunschweig, Germany; m.sinapius@tu-braunschweig.de

[2] Department of Combustion Engines and Flight Propulsion, BTU Cottbus-Senftenberg, 03046 Cottbus, Germany; prechavu@b-tu.de

* Correspondence: h.schmiedeke@tu-braunschweig.de

Abstract: With foil bearings, rotors achieve high rotational speeds with less friction and wear. In addition, here the required space is small and no peripheral components like liquid tanks or pumps are needed. The drawback is a more complex prediction of the real behavior in rotordynamic systems. Impedance test rigs are suitable for investigating the structural-dynamic bearing properties and for validating the theoretical models. This article presents and discusses the measurement of dynamic behavior, i.e., stiffness and damping coefficients, of the structure of a leaf type bearing with undersprings. These measurements include variations in static load due to the relative displacement of the bearing and shaft as well as an attempt to explain the noticed anisotropic behavior of the bearing. This article also shows how much a controlled excitation improves the comparability across the frequency band. For this purpose, a test rig is presented that has been further developed in comparison to known literature approaches. The results show, that the loss factors of the examined bearing structure are up to 4 times bigger below lift-off compared to the operation at 60,000 rpm. Furthermore, the movement amplitudes and the static loads have a great influence on the stiffness and the damping.

Keywords: dynamic coefficients; stiffness; damping; non-rotating; leaf type bearing; non-linear; distortion factor; controlled excitation; test rig

1. Introduction

Aerodynamic foil bearings are increasingly becoming the focus of mobile applications. Drives with fuel cells require high-speed compressors for the intake air. The range of applications in the automotive industry opens up a mass market. Validated applications in turbochargers [1] or in the environmental control system of a Boeing aircraft [2] show good characteristics of the bearings with respect to wear, friction and space requirements. There is no need of fluids and additional devices like oil pumps or tanks. This results in low weights and low costs. However, the biggest disadvantage is the low load-capacity compared to oil lubricated bearings [3]. Therefore, scientists worldwide are researching new bearing designs and looking for improved theoretical models. One concept is the (multi) leaf type bearing, initially developed by Garrett Corporation (USA) [4]. It consists of circular arranged foils, each one bracing direct neighbors. The overall structure is point symmetric. To improve the load-bearing capacity researchers like Heshmat [5], Arakere [6], Silver and Wenban [7], Du et al. [8] or Duan et al. [9] increased the foil stiffness by adding a backing structure below the "leafs". The design varies from nearly undeformed foils [7] to bumps [9] or jagged stripes [5,8].

While some concepts can be described with simpler models but lead to less stiffness improvement, others are much more complex but still promising in regard to stiffness improvement. Heshmat and Heshmat describe for example a theoretical approach to design leaf-type bearings with above mentioned stripes. This includes predictions about

the amount of foils, the right compliance and several other operation parameter [5]. Arakere uses a similar method in [6]. Unfortunately, comprehensive experimental data for leaf-type bearings is missing. Duan et al. discuss mainly the production of leaf-type and bump-type foils for an ø 25 mm bearing. The stiffness of their bearing, calculated from quasi-static force-displacement tests, is between app. 0.9 N/µm for small deflections and goes up to 13.8 N/µm for app. 100 µm shaft displacement [9]. Li et al. explored the influence of structural parameters like the foil thickness, the free foil radius, the foil overlapping ratio and the radial clearance on the load capacity. The tests carried out consisted of a variation in static load on the rotor and the measurement of the shaft eccentricity. Backing structures were not used [10].

A central question with foil bearings is: How to measure the dynamic behavior including the damping? Many scientific work groups use the impedance test rig based on the concept proposed by Childs et al. [11] to observe the frequency-dependent stiffness k and damping c of the foil structure. It consists of two orthogonal measurement axes, each containing an electromagnetic shaker and also sensors to measure acceleration, force and displacement. From the measured data 4 direct and 4 cross-coupled coefficients are calculated (4 × 4 matrix for stiffness and 4 × 4 matrix for damping) [11]. The representation of damping and stiffness curves in a qualitative format will mainly be used for the comparison of the experimental results with the numerical structure models. It is also common to present the results as loss factor as input for rotor dynamic simulations [12]:

$$\gamma = \frac{\Omega \cdot c}{k} = \frac{\Omega \cdot (c_{xx} + c_{yy})}{k_{xx} + k_{yy}} \tag{1}$$

San Andrés and Chirathadam used a test rig with rotating shaft to investigate a metal mesh bearing. They excited the bearing with a sweep sine and showed an inversely proportional relation between stiffness and motion amplitude. However, the average loss factor remained at app. 1 [12]. In another experiment San Andrés and De Santiago used harmonic input signals (single frequency) to achieve maximum shaker efficiency and to lower the error in post-processing due to the higher amplitudes in their oil-film bearing. Applying linear models to non-linear systems is actually only reliable for small movements [13]. The same method was used by Heshmat and Ku to observe the dynamic behavior on their test rig with non-rotating shaft and a controllable static loading device. Their theoretical and experimental results of a bump-type bearing showed a decrease in direct stiffness and damping coefficients with increasing motion amplitude [14]. Rudloff et al. [15] as well as Delgado [16] determined dynamic coefficients at high speeds of an ø 38.1 mm bump-type bearing [15] and a relative big (ø 110 mm) hybrid bearing (combination of hydrostatic and hydrodynamic film pressure) [16]. Rudloff et al. tried to keep a constant excitation force because the coefficients of the investigated bearing were strongly dependent on the frequency and the amplitude of movement. The frequency band investigated ranged from 100 to 600 Hz [15]. Feng et al. focused on the material properties of a combined bump-mesh-type bearing. Therefore the shaft was fixed (non-rotating) and only one measuring axis was used. The calculated loss factor ranged between app. 0.2 and app. 0.6 [17]. A more detailed examination of bump-foils itself has been made by Salehi et al. The foil was mounted in the center of a test rig and dynamically loaded via a shaker. It has been shown that the damping depends mainly on the vibration frequency, the motion amplitude and the applied load [18].

This paper presents and discusses stiffness and damping coefficients of a leaf-type bearing structure with undersprings. The test parameters are inspired by the above-mentioned publications in order to cover the most important influences, i.e., variation of the static load, variation of the motion amplitude and the effect of a force- or a displacement-controlled excitation. The usually neglected non-linear components are quantified here via the distortion factor in order to make statements about the comparability of the results with each other.

2. Materials and Methods

2.1. Test Rig Description

The aim of our research is to focus on the observation of the structural behavior of the foils while disregarding the influence of the lubricant. Usually such tests are performed on test rigs that can also be operated with rotating shafts, as the above mentioned publications show. Therefore, several (auxiliary) bearings and an engine are required. So even if the engine is switched off, the total assembly effects the dynamic behavior of the test bearing. For this reason, the test rig developed and used for our investigations is limited to the essentials: A compact and non-rotating journal mounted on a vibration isolated table (Figure 1). The axis of the journal points in the direction of gravity. This enables to apply any static load, even 0 N without the need of any counter weight. Step strings hold the bearing in order to avoid friction between the outer side of the test bearing and the journal. This pendulum-like mounting guaranties a fixed axial position and allows the bearing to move in radial directions freely. Usually it is achieved with "squirrel cages" or small sticks, which influence the measured stiffness and damping much more [13]. Long strings, on the other hand, do not generate damping, do not transmit bending moments or do not increase the system stiffness in radial directions. In order to minimize static loads due to misalignment, the pendulum center is oriented by plumbing. Similar to impedance test rigs reported in the literature, electromagnetic shakers (K2007E01 PCB Piezotronics Inc., Depew, NY, USA) are connected via 3 turnbuckles to a separate frame. In contrast to rubber mountings, this guaranties a stiff and repeatable vertical alignment while isolating the shaker from vibrations in working direction (low eigenfrequency of the shaker mounting). The plunger coils of the shakers are connected via stingers and impedance heads (288D01 PCB Piezotronics Inc., Depew, NY, USA) to the test bearing. The working resp. measuring axes are placed orthogonal to each other. Instead of drilling holes in the bearing ring or using clamps, the components are linked to the bearing with glued blocks. This avoids deformation of the ring by pre-stresses (clamps) or destructive treatments (holes). Furthermore, the experimentalist can place the blocks freely and re-glue them in small angular steps. The very stiff adhesive DMS X60 has proven to be particularly suitable for this application. Positioning is done with a template.
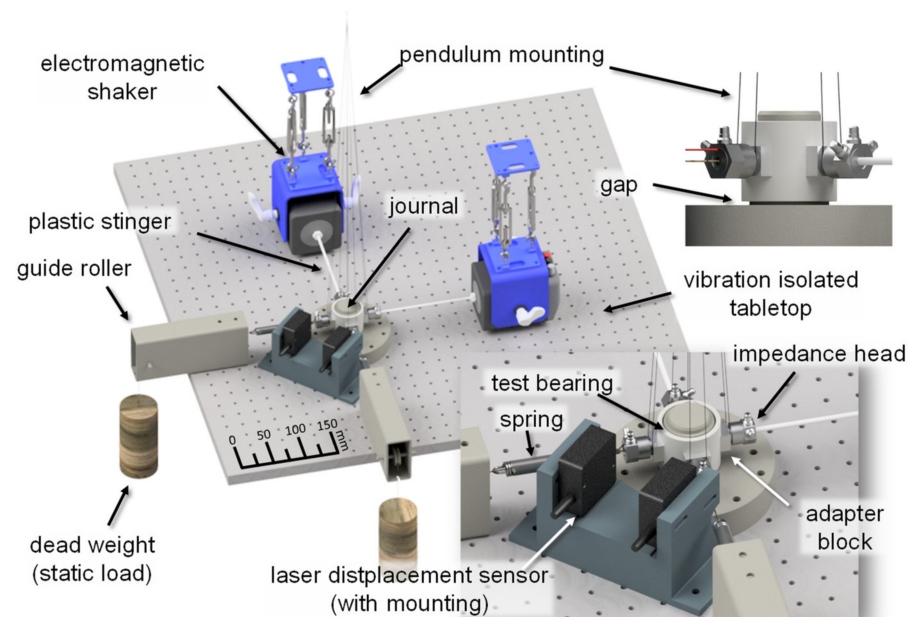

Figure 1. Design of test rig (the dead weights are further away from center than shown: app. 1 m).

An important difference to reported impedance test rigs is the combination of the force and acceleration sensors. Usually the accelerometer is placed on the opposite side

of the bearing ring to align it in the same measuring axis as the force sensor. For this configuration, the bearing ring has to be fully rigid and all mounting planes have to be perfectly parallel to each other. Small deviations inevitably lead to higher measuring errors. A combined sensor minimizes this effect and makes the installation of new test bearings easier. Nevertheless, there are still two identical impedance heads on the opposite side to maintain symmetry. For space reasons, the displacement sensors (M7L/2 WenglorMEL GmbH, Ecching, Germany) are mounted opposite the shakers at 45° angles to the main axes. Templates not displayed in Figure 1 ensure the right alignment of all components in reference to the compact journal and the table bore pattern. After tightening all mounting screws, the stingers are connected and the templates are removed.

The coefficients measured with this test setup are compared in our study below with the results of a conventional test rig. Therefore, the latter is also briefly described at this point.

The test rig consists of an electromagnetic motor, a gear box and a short test shaft running in high precision spindle bearings (XC71903-E) up to 90,000 rpm. The test bearing is centered on the shaft and can move in radial directions freely. End stops on both sides of the test bearing limit axial movement. Figure 2 shows a sectional view of the shaker and the sensor alignment. The piezoelectric force sensors measure the relative forces between the shakers and the outer bearing ring, while the accelerations are measured by sensors on the opposite side. A string with a counter weight compensates the bearing weight including the mounting and sensors weights.
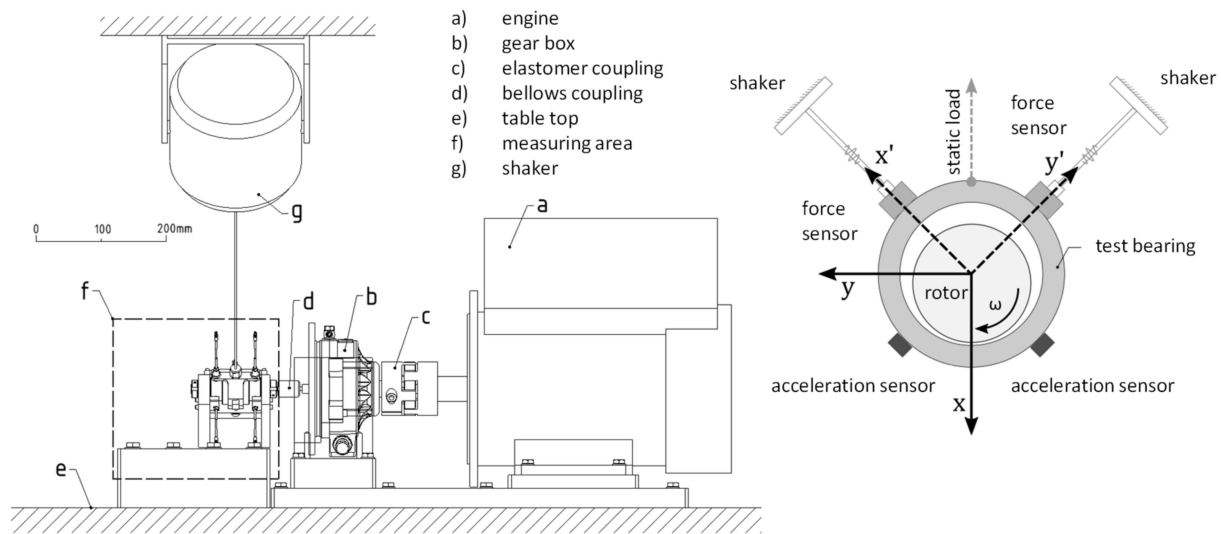

Figure 2. Reference test rig used.

2.2. Experimental Procedure and Parameter Identification

The test procedure and subsequent data analysis of our self-developed test rig itself corresponds to the publications [14–16,19,20]. The controller generates harmonic signals for each shaker individually, which results in two different measurements per frequency required to solve the 2-dimensional equation system based on the 2-mass oscillator (Figure 3) consisting of the bearing mass m_b and the table plate mass m_t stored on an air cushion. The following equation describes only the bearing specific forces due to the bearing motion (u_b) and the table or journal motion (u_t). The table plate mass m_t is not required:

$$\begin{bmatrix} m_{xx} & m_{xy} \\ m_{yx} & m_{yy} \end{bmatrix}_b \cdot \ddot{u}_b + \begin{bmatrix} c_{xx} & c_{xy} \\ c_{yx} & c_{yy} \end{bmatrix}_b \cdot \dot{w}_{b-t} + \begin{bmatrix} k_{xx} & k_{xy} \\ k_{yx} & k_{yy} \end{bmatrix}_b \cdot w_{b-t} = F \tag{2}$$

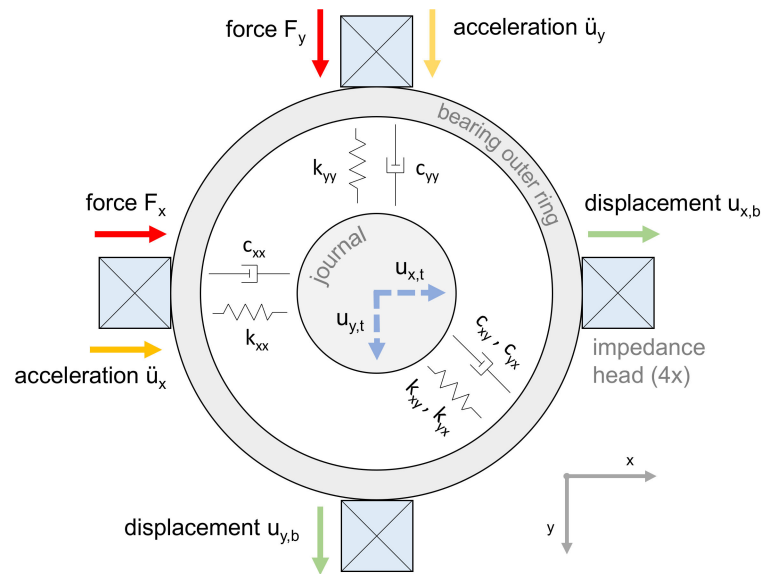$$with: \; w_{b-t} = u_b - u_t \; and \; u, w, F \in \mathbb{C}^{2x2}$$

Figure 3. Simplified 2D model for the data evaluation.

The measured force F as well as the acceleration ü are related to the bearing ring. The displacement w_{b-t} is relative between the journal (table top) and the bearing. In case of even small displacements of the tabletop (incl. journal) u_t, the motion of the foils (w_{b-t}, $\dot{w}_{b-t}$) has to be taken from the displacement sensor (instead of integrating the acceleration data). Furthermore, each harmonic sensor signal consists of constant amplitude r_{ln} and phase information ϕ_{ln} besides the dynamic term $e^{j\cdot\Omega\cdot t}$. Ω is the excitation circular frequency and t the current time. As a simplification, the characteristic parameters (r_{ln}, ϕ_{ln}) are summarized in matrices for the relative displacement $\hat{w}_{b-t}$, the force $\hat{F}$ and the acceleration $\hat{\ddot{u}}$:

$$\left\{ \begin{array}{cc} w_{xx} & w_{xy} \\ w_{yx} & w_{yy} \end{array} \right\}_{b-t} = \left\{ \begin{array}{cc} r_{w,xx}\cdot e^{j\Omega t + j\phi_{w,xx}} & \cdots \\ \cdots & \cdots \end{array} \right\}_{b-t}$$

$$= \left\{ \begin{array}{cc} \left(r_{w,xx}\cdot e^{j\phi_{w,xx}}\right)\cdot e^{j\Omega t} & \cdots \\ \cdots & \cdots \end{array} \right\}_{b-t} = \hat{w}_{b-t}\cdot e^{j\cdot\Omega\cdot t} \quad (3)$$

$$and \; \dot{w} = j\cdot\Omega\cdot w$$

$$F = \hat{F}\cdot e^{j\Omega t} \quad (4)$$

$$\ddot{u} = \hat{\ddot{u}}\cdot e^{j\Omega t} \quad (5)$$

After inserting the terms in Equation (2) and reducing $e^{j\Omega t}$ the formula shows

$$k_b + c_b\cdot j\Omega = \left(\hat{F} - m_b\cdot\hat{\ddot{u}}_b\right)(\hat{w}_{b-t})^{-1} \quad (6)$$

The Fourier transformation of the raw sensor data provides the complex values $\hat{F}$, $\hat{\ddot{x}}_b$ and $\hat{w}_{b-t}$. Using swept sine instead, as described in the most publications and used in the reference test rig, leads to a superposition of linear and non-linear amplitudes and phase information in the response signals [21,22]. Therefore, it is important to assess all results with the underlying distortion factors, especially because new bearing configurations with e.g., undersprings or uneven bump heights may increase the non-linear behavior.

The evaluation method is implemented in Labview 2017 and contains a fully automatic test modus as well as the post-processing including the calculation and presentation of the dynamic coefficients. Each test has its own sampling rate depending on the excitation frequency (24 samples per period) and lasts for 10 s. The post-processing removes the

first and last part of the raw data to get the settled behavior. The graphs below are based on data chunks of 50 periods. Afterwards the software uses a flat-top window and DFFT to calculate the dynamic coefficients (Equation (6)). Similar to publication [14], only the frequencies of the excitation were used. With respect to [12,17,23], the impedance test rig has an excitation controller to get comparable results. Therefore, the experimentalist has to set the desired target value for the force [N] or the displacement [μm]. Before starting each measurement, the module uses a loop of sequences of immutable sine excitations followed by a Fourier transformation to determine the new input amplitude to reach the target value. Previous values serve as initial values. Thus, one sequence can last between 5 s to approx. 30 s to reduce the error relative to the target value below a user defined limit (here 1%). The drawback of this relatively time consuming procedure is that the coating of the test bearing (in this case the PTFE based coating between the leaf foils and the journal) could wear out. To avoid significant changes in properties, there are only a few frequency steps per parameter variation in the test results below. To check the reliability, the parameter variations are repeated after several test sequences with other parameters. In case of the leaf type bearing no visible drift has been discovered. Long-term tests were not carried out.

2.3. Test Bearing Description

The investigated leaf type bearing (Table 1) consists of 8 foil pairs of leaf foils (or "top foil") and underspring foils. Both are made of spring steel. The shaft diameter is 35.55 mm and its width 40 mm. A teflon-based coating on the foils improves the dry friction before lift-off. This also has a positive effect on the installation of the test bearing, as friction between journal and leaf foils caused by the preload must be overcome.

Table 1. Parameter leaf-type bearing.

Parameter	Dimension
Shaft diameter	35.5 mm
Bearing housing inner diameter	36.7 mm
Bearing length	40 mm
Foil thickness (leaf, underspring)	0.12 mm
Coating thickness	0.02 mm
Number of leaf foils	8
Foil Young's Modulus	185 GPa (1.4310)
Foil Poisson's ratio	0.29
Leaf foil angle	app. 75°
Underspring angle	app. 38°
relative clearance	0.0087

Without any additional static load, the bearing is expected to behave point-symmetrically. Any further load (Figure 4) leads to an uneven deformation of the foils. In case of the shown static force direction the foil 8 is clamped at the foils free end and the foil 2 is clamped in the middle. Besides that, the leaf and the underspring foils do not cover multiples of 45°. The stiffness and damping in x- and y-direction should be different as expected.

The bearing has 4 main friction contacts (Figure 5), which can be clamped on both sides (first detailed view) or loaded on one side (second detailed view). The undersprings are in contact with the outer ring at least one more time in addition to the fixed position (last detailed view) and have a damping effect here due to the friction. The leaf foils are also supported at least twice on the undersprings (one end is fixed and thus blocked in movement). Thus, a leaf foil has at least 4 friction contacts, the previously discussed contact between the journal and the running film is already included. The figure also shows the presumed evasive movement of the foils when the journal and bearing move relative to each other. With the form of motion present on the test rig, all contacts should therefore rub against each other at the same time. Due to the different angles between the evasive movements, however, different blocking forces for each contact are to be expected.
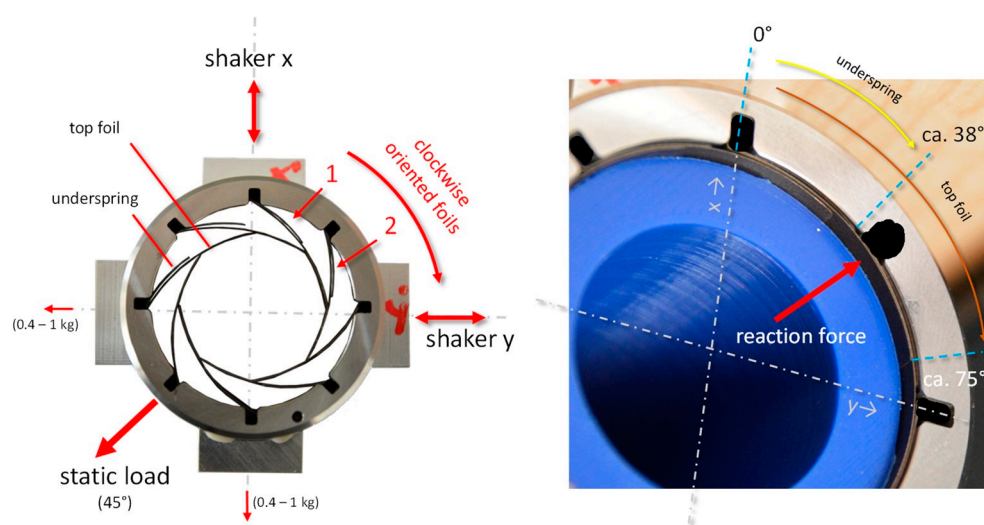
Figure 4. Top view of the tested leaf type bearing (**left**); leaf foil angular length and bearing ring motion (**right**).
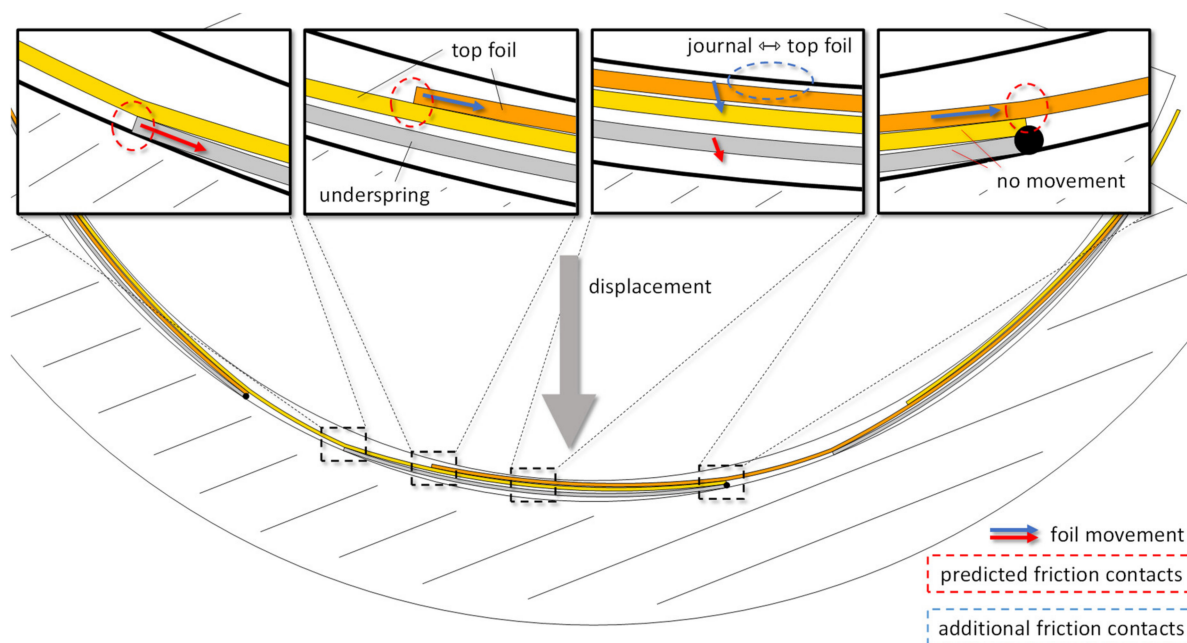

Figure 5. Contact zones between the journal, the foils and the bearing ring (true to scale).

3. Results

The tests described below show the influence of the static loads (0.4 to 1 kg per axis), the difference in controlling (force or displacement) and the stick-slip effects. The first attempt to identify the right parameters is displayed in the hysteresis curves in Figure 6 and the stiffness data in Figure 7. The hysteresis curves contain the measured raw data of one measurement without any windowing or Fourier transformation. To avoid random measurement errors 50 periods where superimposed and averaged. Each point thus represents the averaged force and displacement that were present at the same time within a period. The frequency band (100 Hz to 500 Hz) was divided into 60 steps as a compromise between measurement duration and frequency resolution. The selection of hysteresis curves in Figure 6 is limited to the frequencies where changes are visible. In order to find suitable start parameters, the force amplitude was increased until the first uniform

oscillations were present in the lower frequency range (10 N). A more detailed description can be found in Appendix A.
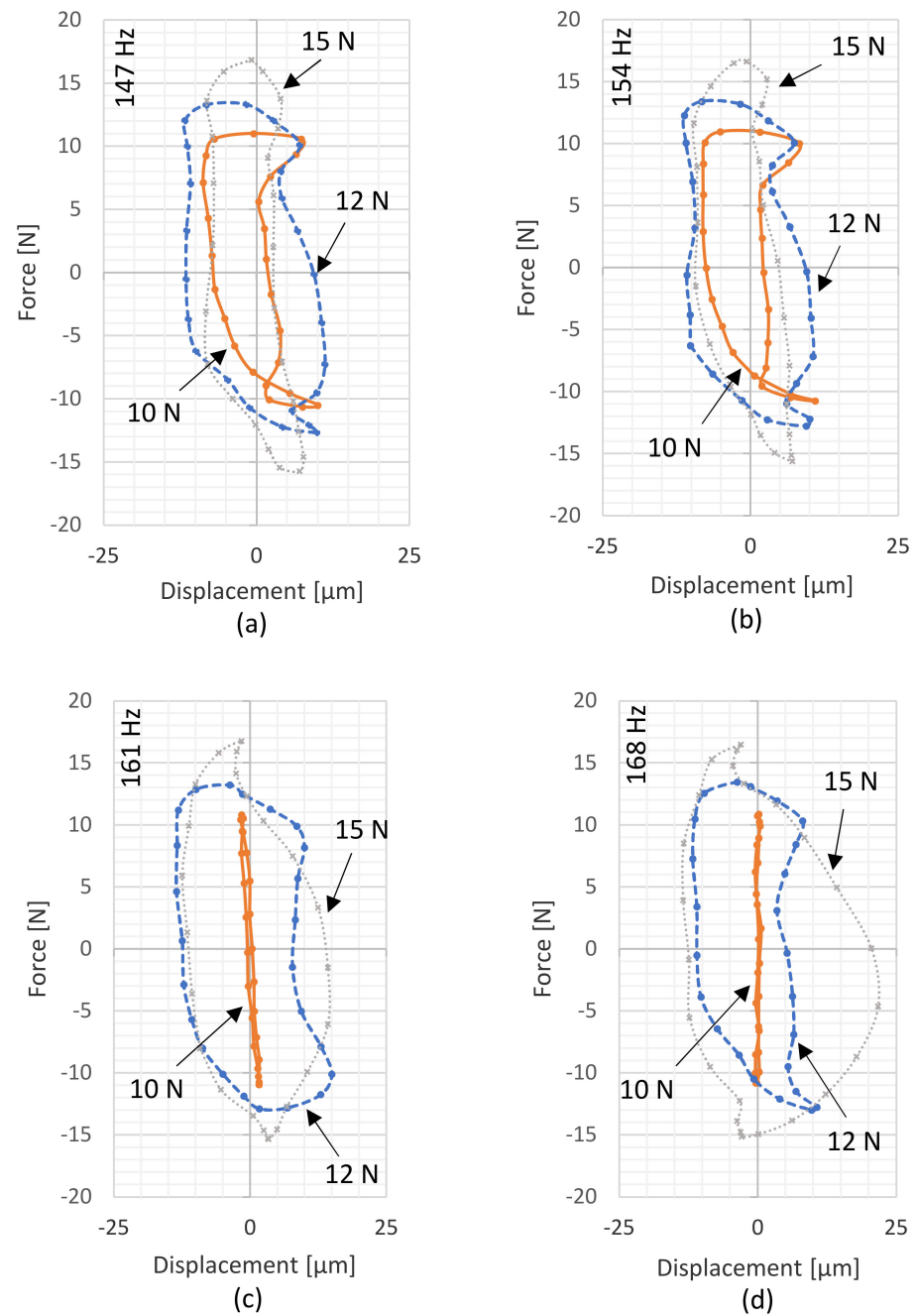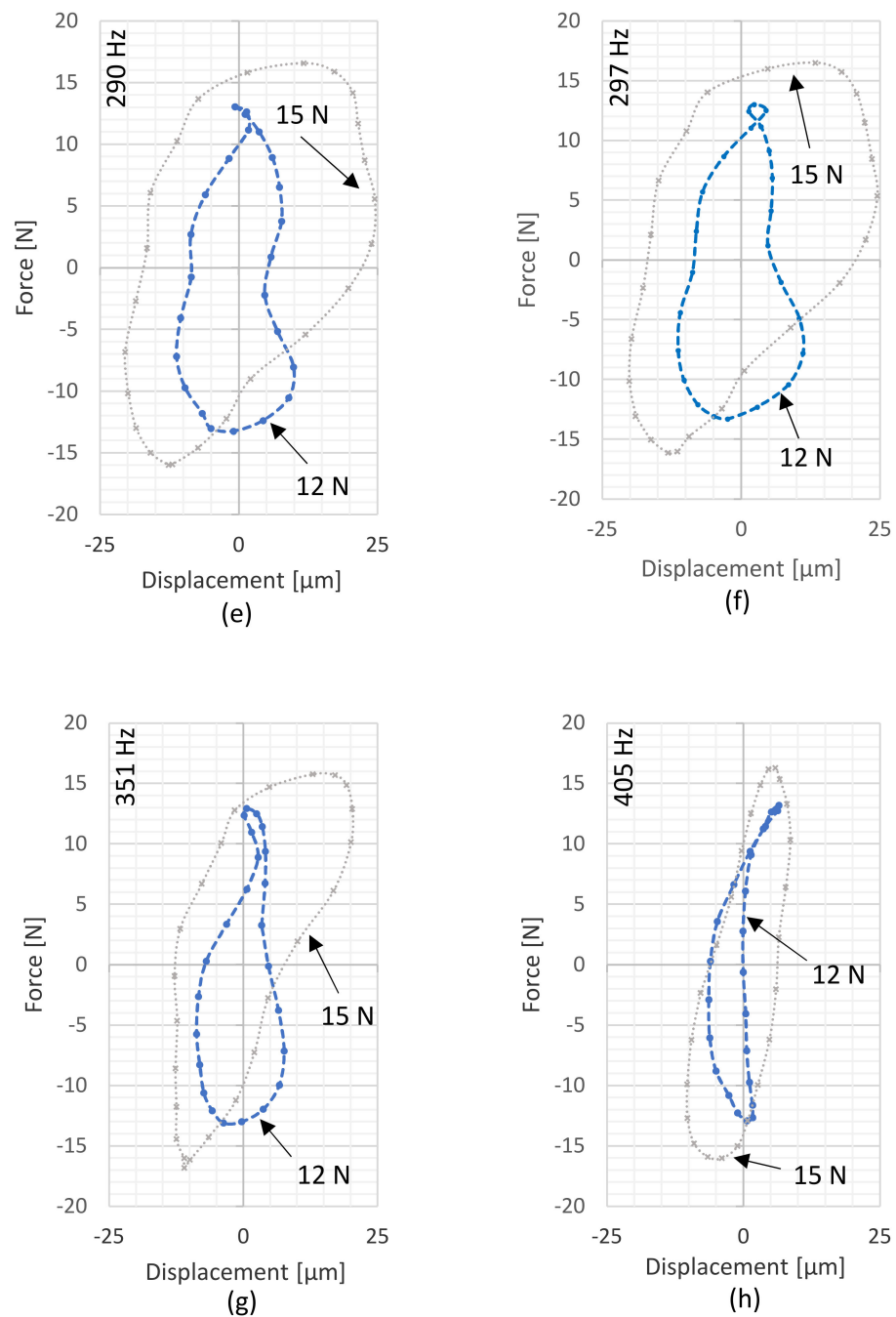

Figure 6. *Cont*.

Figure 6. Averaged hysteresis curves (xx-direction) showing the dependency of force (ca. 11.1 N static load) from 147 Hz to 405 Hz (**a**–**h**).

At 10 N and a static load of ca. 11.1 N, friction between 161 Hz (squeezed ellipse) and 168 Hz (straight line) starts to completely block the foil movement (see the collapse of the hysteresis curve). This blocking leads to a stiffer bearing and increases the eigen-frequency. If the force is slightly above the static friction, sudden stiffness jumps due to the break free (followed by consecutive stick-slip effects) occur, causing non-linear vibrations. Furthermore, it should be noted that this extreme small movements can hardly be detected by the sensors and are overshadowed by noise (despite averaging). This is why the ideal elliptic hysteresis curves become more and more deformed as the force amplitude decreases or the frequency increases, i.e., the ratio of inertia force to force increases—so the displacement amplitude decreases, even if the force keeps constant. The stiffness curves in Figure 7 sum up the behavior quite accurate. Continuous curves are measured up to

the individual blocking frequency, followed by large jumps. The difference between the force levels is particularly visible in x direction. The maximal values are greater and the stiffness decreases significantly at higher force amplitudes. Thus, it is absolutely necessary to define a minimum force or displacement amplitude to avoid big distortion factors d_{ln} of each direction. Distortion factors describe the impact of super harmonic vibrations on the signal [24]:

$$(d_{ln} =) d = \frac{\sqrt{I^2 - I_1^2}}{I^2} \ with \ I = \sqrt{I_1^2 + I_2^2 + I_3^2 + \dots} \ and \ l, n \in \{x, y\} \tag{7}$$
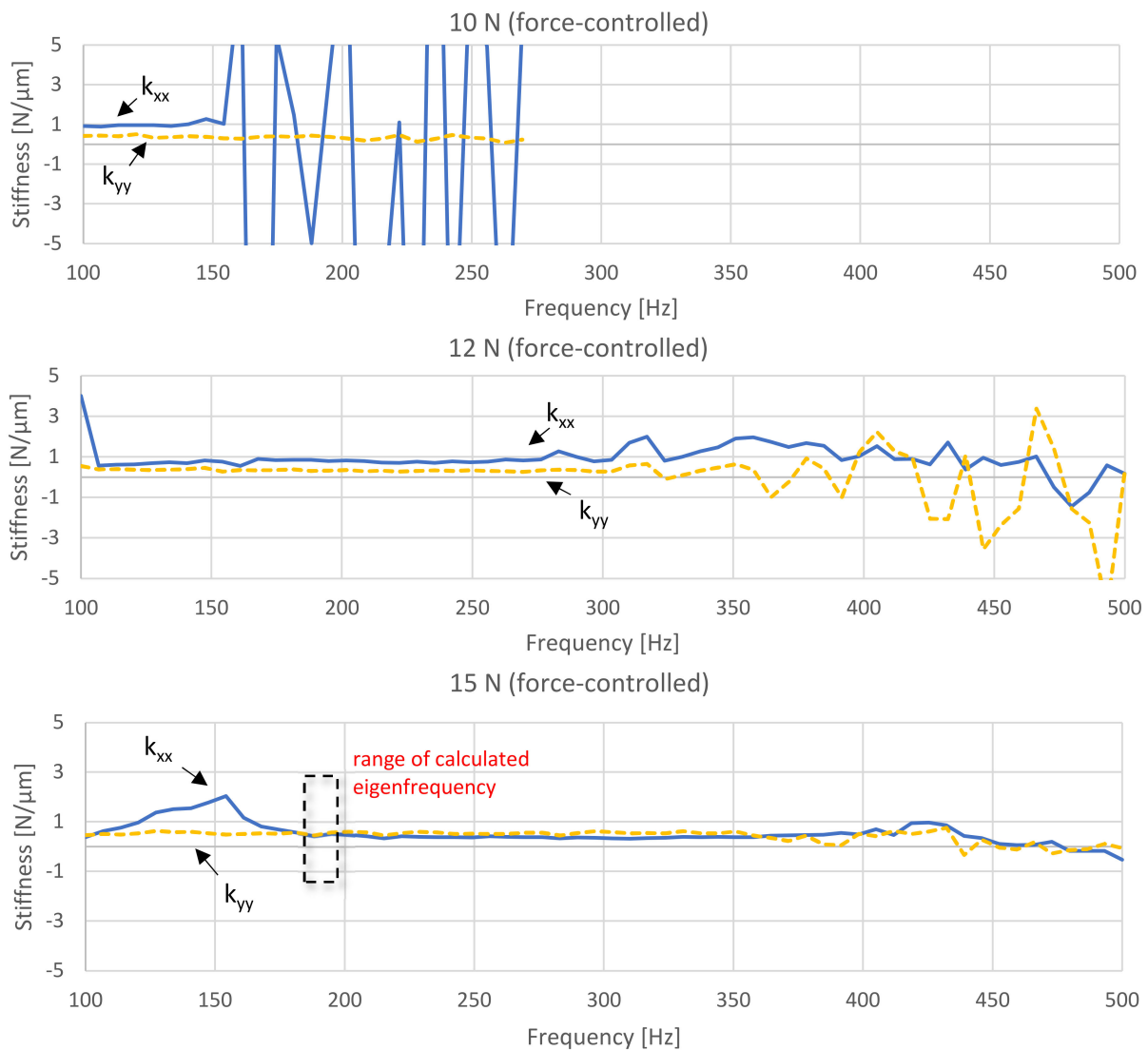

Figure 7. Force-controlled pre-tests: 10 N (**top**), 12 N (**center**), 15 N (**bottom**).

In case of sinusoidal (harmonic) curves, the root-mean-square I (index is equal to order of super harmonics) depends linearly on the amplitude $\hat{\imath}$ [24]; this also counts for the amplitudes r in the sensor signal parameters $\hat{F}, \hat{u}_b, \hat{w}_{b-t}$:

$$I = \frac{\hat{\imath}}{\sqrt{2}} with \ \hat{\imath} \in \{r_{F,ln}, r_{\ddot{u},ln}, r_{w,ln}\} \ and \ l, n \in \{x, y\} \tag{8}$$

The comparison of the hysteresis curves of 12 N and 15 N at 161 Hz as well as the distortion factors d_{ln} presented in the Figure 8 show that the sharp peaks of the shape disappear with distortion factors d_{ln} at app. 25%. The related stiffness values (15 N force amplitudes) for distortion factors below that threshold are $k_{xx} \approx 0.5$ N/µm and $k_{yy} \approx 0.4$ N/µm. Calculating the eigenfrequency of the test bearing (mass of all moving parts: 350 g)

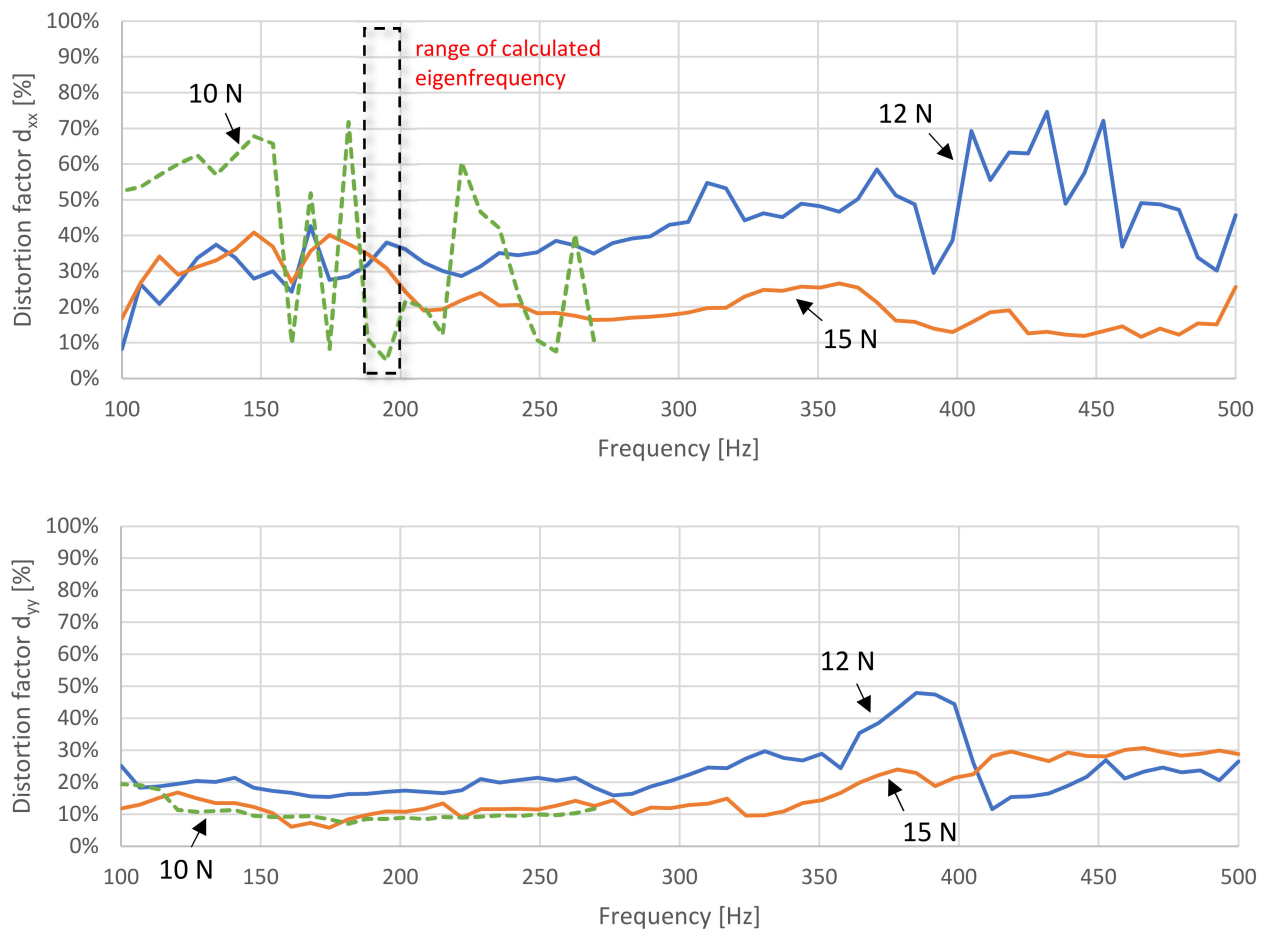$$f = \frac{\Omega}{2\pi} = \frac{1}{2\pi}\sqrt{\frac{k}{m}} \tag{9}$$

Figure 8. Distortion factors d_{ln} of the pre-tests (11.1 N static load).

Leads to a frequency range right below 200 Hz (Figures 7 and 8). Herein, the phase difference of force and motion decreases and the sign subsequently reverses (see tilting of the hysteresis curves in Figure 6). Due to its self-reinforcing nature, this area should be examined carefully.

As a consequence of these findings, Figure 9 displays only the acceptable range from app. 200 Hz to 350 Hz. The stiffness remains almost constant in this range, while the damping shows a quadratic curve (see dotted regression curves and related equations). The stiffness and damping in y direction are nearly 0.2 N/µm and 80 Ns/m (200 Hz) to 400 Ns/m (350 Hz) larger than in x direction. Additional measurements with displacement controlling (Figures 10 and 11) induce slightly decreasing stiffness (linear) and damping curves (x^{-1}). The regression curves for these diagrams are calculated from data averaged from three successive measurements with a static load of app. 8.3 N. The stiffness k_{xx} has nearly the same gradient and value (app. 0.1 N/µm deviation) for app. 5.5 N up to 11.1 N static load whereas k_{yy} depends greatly on the static load. At 200 Hz the difference between

5.5 N to 8.3 N and 8.3 N to 11.1 N is app. 0.1 N/µm each. Until 360 Hz this difference halves. The same observation is notable for the damping. The deviation of c_{yy} for 5.5 N to 8.3 N and 8.3 N to 11.1 N is about twice (app. 100 Ns/m) as large as for c_{xx}.
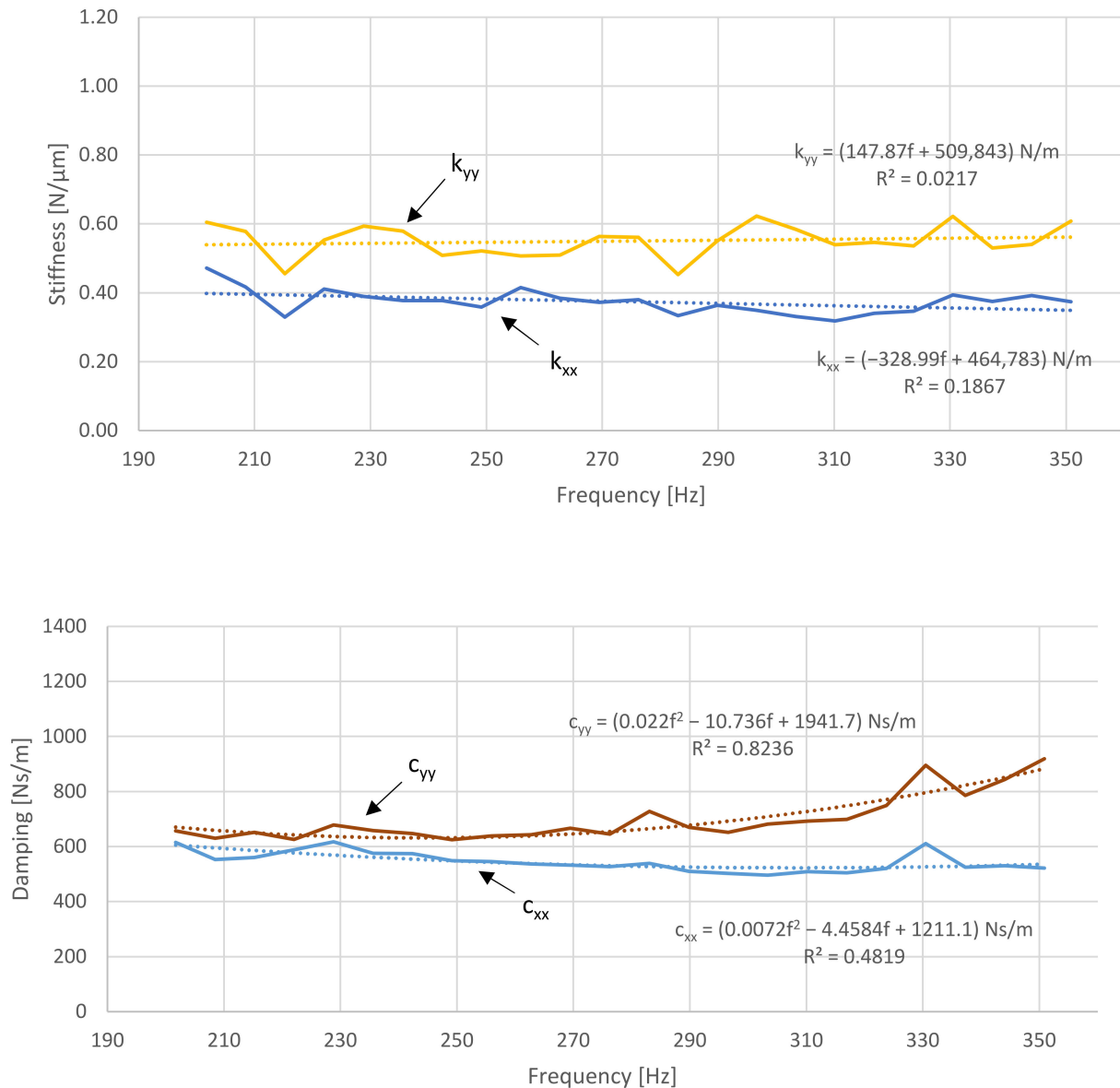

Figure 9. Dynamic coefficients with friction factors below 25% (200 Hz–350 Hz); 15 N dynamic force amplitude; 11.1 N static load.

The variance of the data points (e.g., in Figure 9) are mainly due to the error in controlling the force amplitude (see variance of force amplitude between 14.7 N to 15.2 N in Figure 12). However, it must be noted that each measured point in the diagrams depends on several boundary conditions that could force the non-linear system to behave completely differently! Strictly speaking, these data points can therefore not be approximated with gradients. It is noticeable, however, that despite non-linearity and despite the discussed influencing parameters, trends are reflected in the measured data (see fitted curves).
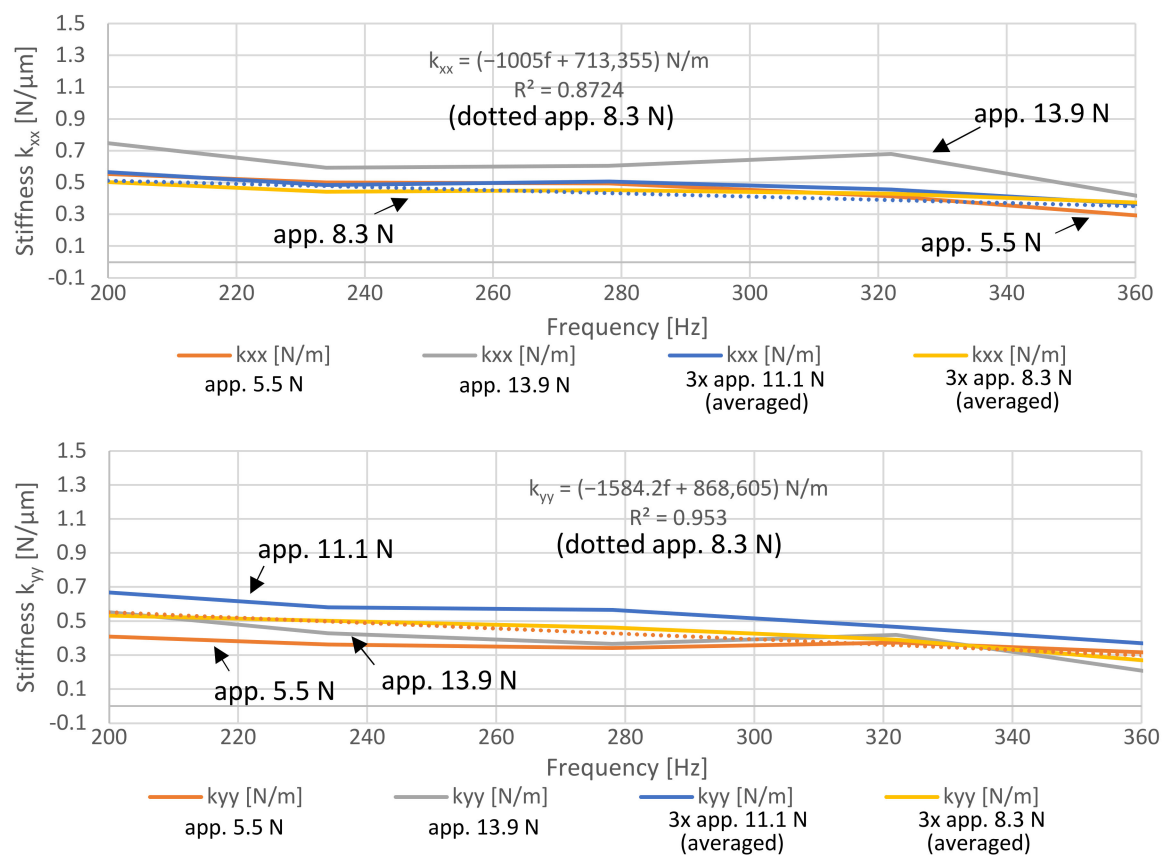
Figure 10. Stiffness: Displacement controlled (20 μm); changing static loads between app. 5.5–13.9 N.

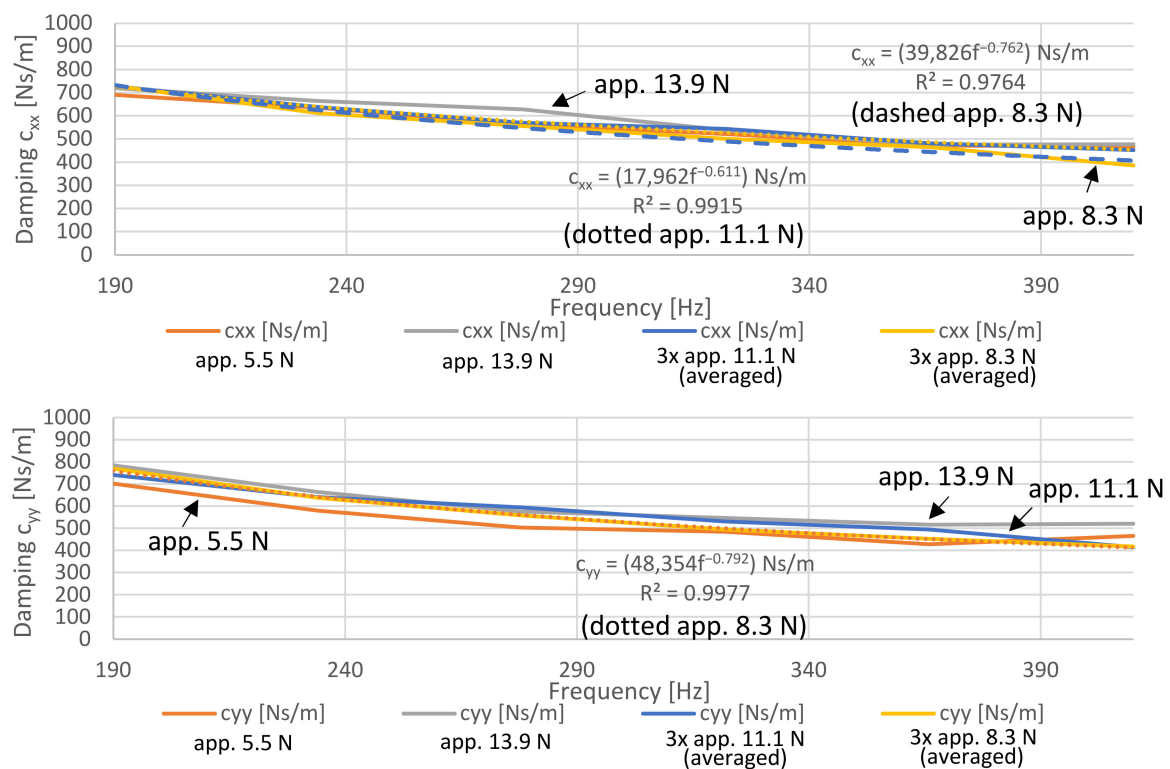**Figure 11.** Damping: Displacement controlled (20 μm); changing static loads between app. 5.5–13.9 N.
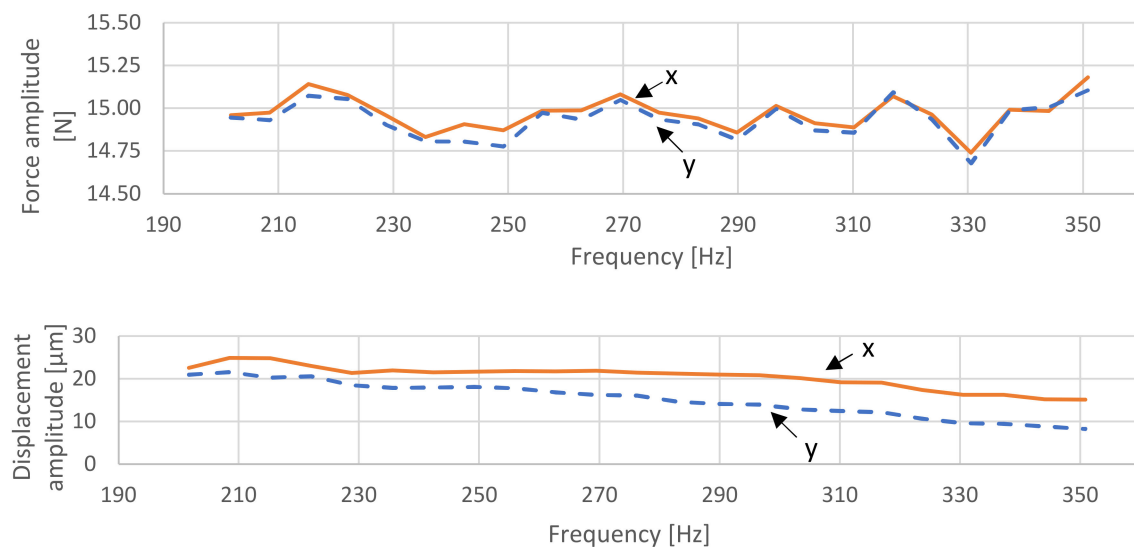
Figure 12. Main force amplitude (**top**) and displacement amplitude (**bottom**) of measured sensor data of pre-tests with 11.1 N static load and 15 N force amplitude (only synchronous).

Figures 13 and 14 display data collected while changing the target value from 6 μm to 20 μm. The small displacement amplitudes lead to high distortion factors (similar to the discussed force control) shown in Figure 15 whereas 14 μm and 20 μm have a similar non-linear vibration behavior. It is noticeable that greater displacements cause lower stiffness (ca. 0.2 N/μm) and damping values (ca. 250 Ns/m). The reasons may be initial forces inside the foils (reduced normal forces), a non-linear behavior of the coating between the journal and the top foils, and a non-linear angular change of the direction of the evasive foil movements due to the deflection of the foils (Figure 5). The friction itself was assumed to be independent of speed (coulomb friction) [2].
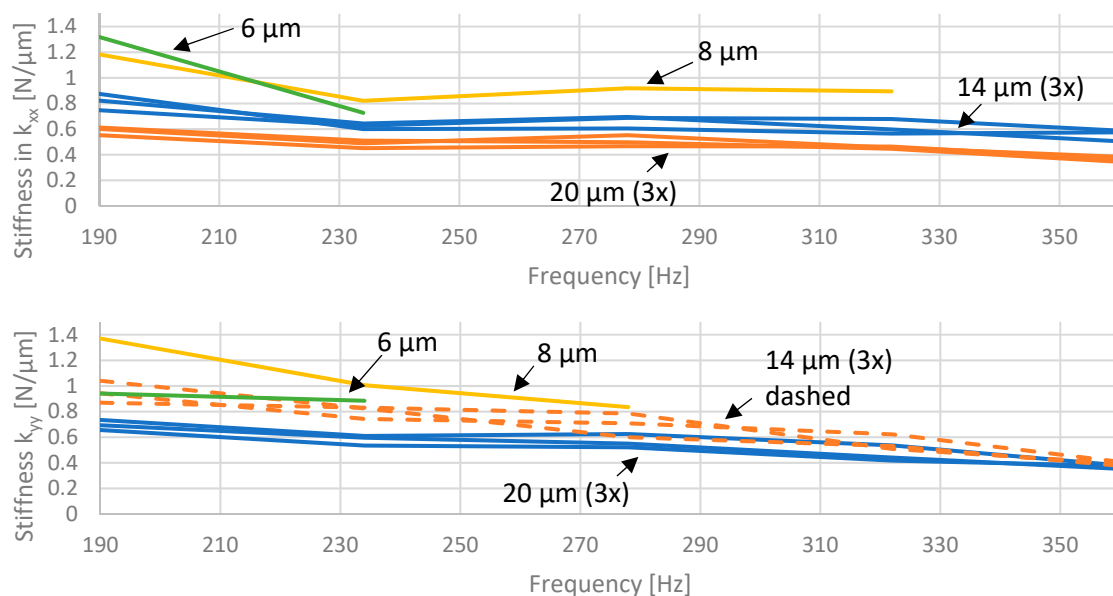

Figure 13. Influence of different displacement amplitudes on direct stiffness coefficients at 11.1 N static load; tests with 6 μm and 8 μm were stopped due to poor control behavior (highly non-linear); repeated measurements (3 times) including new controlling sequences (see error discussion of controller).

Figure 14. Influence of different displacement amplitudes on direct damping coefficients at 11.1 N static load; tests with 6 μm and 8 μm were stopped due to poor control behavior (highly non-linear); repeated measurements (3 times) including new controlling sequences (see error discussion of controller).
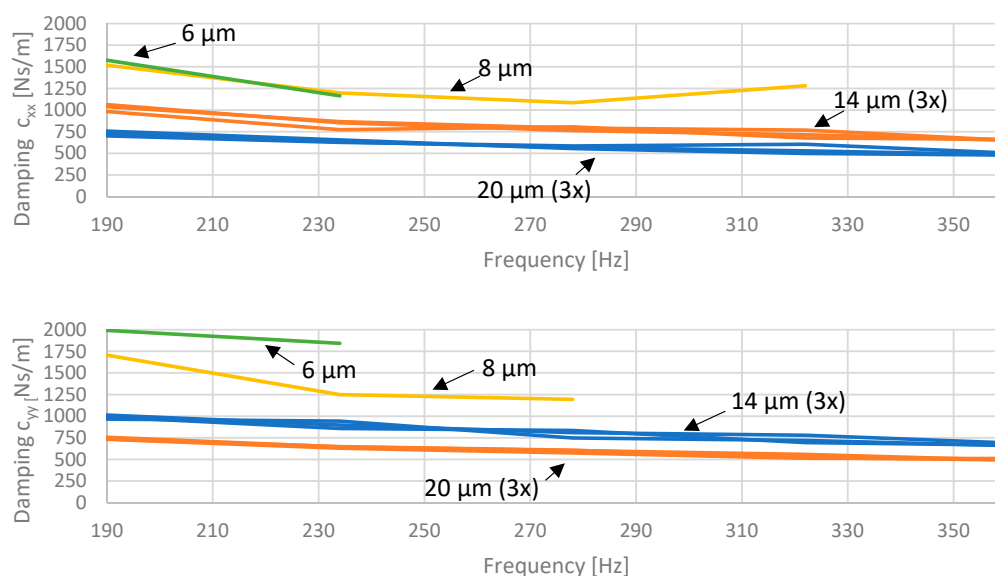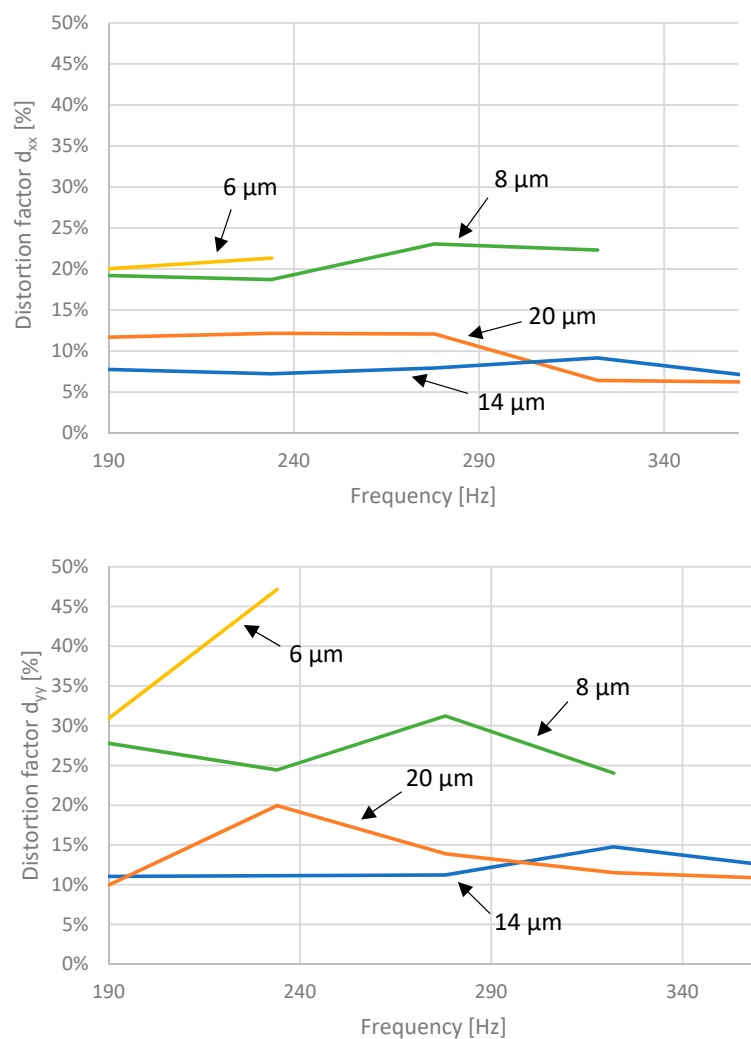

Figure 15. Distortion factors of tests at different displacement amplitudes (6–20 μm); 11.1 N static load.

The changing static load has a small impact in x-direction and an obvious one in y-direction. Loads between approx. 5.5 N and 11.1 N have a similar effect: the difference of stiffness in x is approx. 0.05 N/µm, whereas a static load of approx. 13.9 N seems to lead to an overload with almost no foil deflection in x-direction. The orthogonal direction is more prone to the variation of loads and shows changes of 0.3 N/µm in stiffness. The reason lies in the asymmetry due to static loads mentioned above. The preload causes friction and prevents the evasive movement of the foil ends, whereas foil 8 seems to be nearly blocked with all chosen loads the movement of foil 2 has a bigger range from freely sliding to a disabled condition (foil numbering see Figure 4). Furthermore, higher loads tend to lead to higher stiffness and damping values. Although the curves of approx. 5.5 N contradict this statement, they only consist of one measurement instead of the average of at least three measurements like the curves of ca. 8.3 N and ca. 11.1 N. In contrary, a static load of ca. 13.9 N seems to be mainly supported by the end of foil 8 and leads so to a huge difference in x- and y-direction.

4. Discussion

However, how to compare the results obtained by a force- or displacement-controlled test? As it turned out, calculating the loss factor for each measurement leads to a similar trend (Figure 16). The loss factor, which is given by the relation between damping and stiffness (Equation (1)) increases with frequency. The diagram also shows the impact of static load which causes greater relative differences in stiffness as in damping. More preload results in smaller values. Furthermore, the relation between displacement and friction discussed above causes greater incline of the force-controlled result $\gamma_{11.1 \text{ N, } 15 \text{ N}}$ (the first index describes the static load and the second the target value for controlling) compared to the displacement-controlled curves $\gamma_{8.3 \text{ N, } 20 \text{ µm}}$ and $\gamma_{11.1 \text{ N, } 20 \text{ µm}}$. The intersection point of $\gamma_{11.1 \text{ N, } 15 \text{ N}}$ and $\gamma_{11.1 \text{ N, } 20 \text{ µm}}$ should be at 0 Hz because of the same static load condition (11.1 N). Considering the results in Figure 16 this is plausible.
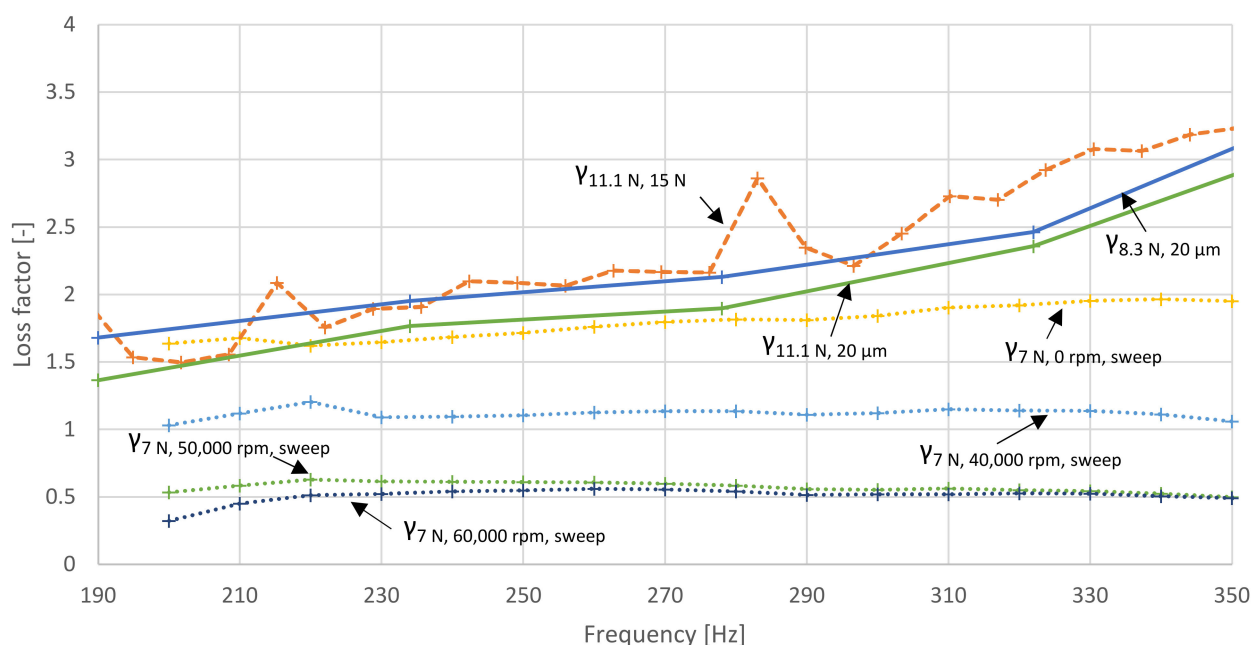

Figure 16. Comparison of loss factors (Equation (1)); first index: static load; second index: controlled force (N) or displacement (µm) amplitude or results from different rotation speeds.

Unfortunately, there are hardly any comparable publications of experimental results of leaf-type bearings. However, it is known that similar dimensions of bump-type bearings for example induce loss factors of ca. 0.25 [15] and of metal mesh bearings induce loss factors of 0.8 to 1.5 [12]. A reported experiment with bump-type dampers [18] also shows

the above described dependencies on the displacement amplitudes, the static loads and the frequency on the damping.

The calculated loss factors in this article are surprisingly high and should lead to a bad lift-off. For the verification and to determine the influence of the foil-shaft contact results of a conventional test rig were used. Figure 16 shows a reduction of the loss factor with higher rotation speeds. Below lift-off (app. 32,000 rpm tested with app. 5.7 N) the loss factor is between 1.6–2 and drops to 0.45–0.56 (excl. sweep start frequency) at 60,000 rpm. There is just a small difference between the two highest speeds. The air film has stiffened up.

It should be noted that there are slight differences between both test rig setups and the angular direction of the static load. Therefore, the loss factors calculated from the conventional test rig and from the new one cannot be perfectly equal. This can also be observed in the results (Figure 16), which are derived from the Figures 10 and 11. Most similar are the results for the 0 rpm conventional test (7 N) and the displacement controlled test $\gamma_{8.3\,N,\,20\,\mu m}$ (8.3 N). It should be noted that the conventional test rig had no displacement or force controller. Therefore, it is plausible that the results of both test rigs show in some areas conformity (200–280 Hz: deviation < 15%) and in other areas greater deviation. Nevertheless, both test methods show large loss factors and so predict a relative high lift-off speed.

5. Conclusions

This study shows the influence of displacement and static force in a typical leaf-type bearing structure with undersprings below lift-off. In case of the tested bearing structure displacement amplitudes have significant impact on stick-slip and the blocking of friction contacts resulting in non-linear motion responses. Therefore, slight deviations in excitation could lead to incomparable dynamic coefficients. To reduce the error, the displacement amplitude should be kept constant for each frequency of a measurement. The results also show, that a prediction of the structural dynamic behavior below lift-off is not possible just from impedance tests with lifted shaft. The loss factor is highly depending on the preload and on the surfaces in the shaft-foil contact zones. Compared to the lifted shaft with stiff air film the loss factor is 3 to 4 times greater. However, it has also been shown that further tests with different coatings and preloads are necessary in order to be able to correctly simulate and predict the bearing behavior up to lift-off. The shaft-foil contact in particular should be investigated more specifically.

Author Contributions: Investigation, H.S.; investigation on "conventional" test rig, sketch of that test rig, N.P.; writing, H.S., M.S.; project management, scientific consulting and paper review, M.S. All authors have read and agreed to the published version of the manuscript.

Institutional Review Board Statement: Not applicable.

Informed Consent Statement: Not applicable.

Data Availability Statement: Data is contained within the article.

Conflicts of Interest: The authors declare no conflict of interest.

Abbreviations

app.	approximately	
Φ	phase of signal	[rad]
Ω	circular frequency	[rad/s]
F	force	[N]
$I,\ i$	(RMS) current	[A]

b (*index*)	related test bearing	
c	damping	[Ns/m]
d	distortion factor	[-]
f	frequency	[Hz]
j	complex number	[$\sqrt{-1}$]
k	stiffness	[N/m]
m	mass of moving parts	[kg]
RMS	root-mean-square	
t	time	[s]
t (*index*)	related to table/journal	
u	displacement	[m]
w	relative displacement between bearing and journal	[m]
xx, *xy*, *yx*, *yy*(*index*)	first letter: direction of excitation seconds letter: direction of measurement	
γ (*gamma*)	loss factor	[-]

Appendix A

This appendix serves as a supplementary explanation of the hysteresis curves, the chosen frequencies and the choice of the force amplitudes for the force-controlled tests under 11.1 N static load. Therefore, the following figures (Figures A1–A3) show waterfall plots of the sensor data (windowed with flat top) between 3 s and 3.5 s in x-direction. The data before this are neglected due to the transient effect. The offset (0 Hz) was also removed. Finally, the harmonic (x1) and the first two super harmonics (x2, x3) were identified in the diagrams.

The comparison of the force amplitudes between the three tests (10 N, 12 N and 15 N) shows that the controlled amplitude could be maintained from 100 Hz to 500 Hz and that the super harmonic amplitudes are less than app. 5% of the harmonic amplitudes. However, there are 2 peaks in x2 (app. 200 Hz) and x3 (app. 310 Hz). The first could be related to the eigenfrequency of the bearing (slightly below 200 Hz; see Equation (9)).

In contrast to the force signal, the super harmonic displacement amplitudes are partly half the size of the harmonic displacement amplitudes. Furthermore, Figure A1 shows a sudden shift at 161 Hz from uniform vibrations (with app. 7 μm) to alternately blocked or reduced movement (around app. 2 μm). Small disturbances could be the reason for this, which cause the contacts to break up (e.g., 181 Hz and 221 Hz). With the change to 12 N force amplitude (Figure A2), the behavior has stabilized up to 500 Hz. However, larger fluctuations in the displacement amplitudes shortly before 300 Hz and from app. 350 Hz are noticeable and suggest partially blocked contacts. The frequencies of the hysteresis curves in Figure 6 were selected accordingly. Figure A2 also shows almost twice as high displacements compared to Figure A1. A further doubling occurs at force amplitudes of app. 15 N (Figure A3). The largest values are at app. 100 Hz (app. 38 μm) and between 201 Hz and 214 Hz (app. 35 μm). The second maximum also seems to be linked to the eigenfrequency of the bearing. Furthermore, the amplitude curve x1 is smoother as in Figure A2. In order to prevent critical resonance, the force amplitude was not increased further.
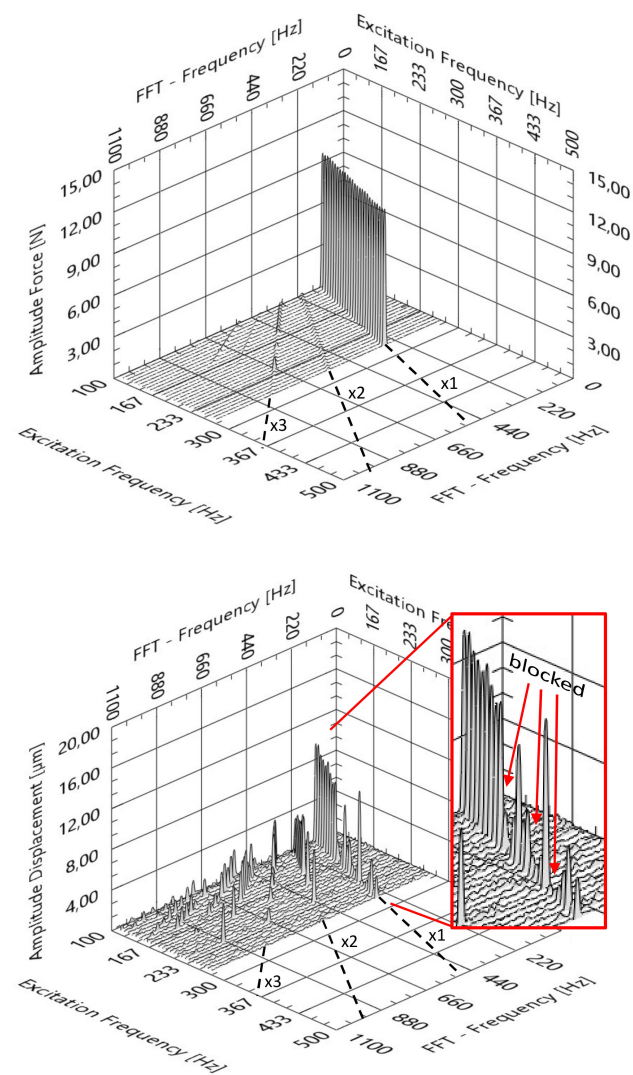
Figure A1. Waterfall plot of force and displacement sensor data in x-direction (11.1 N static load, 10 N force amplitude); cancelled at app. 269 Hz.
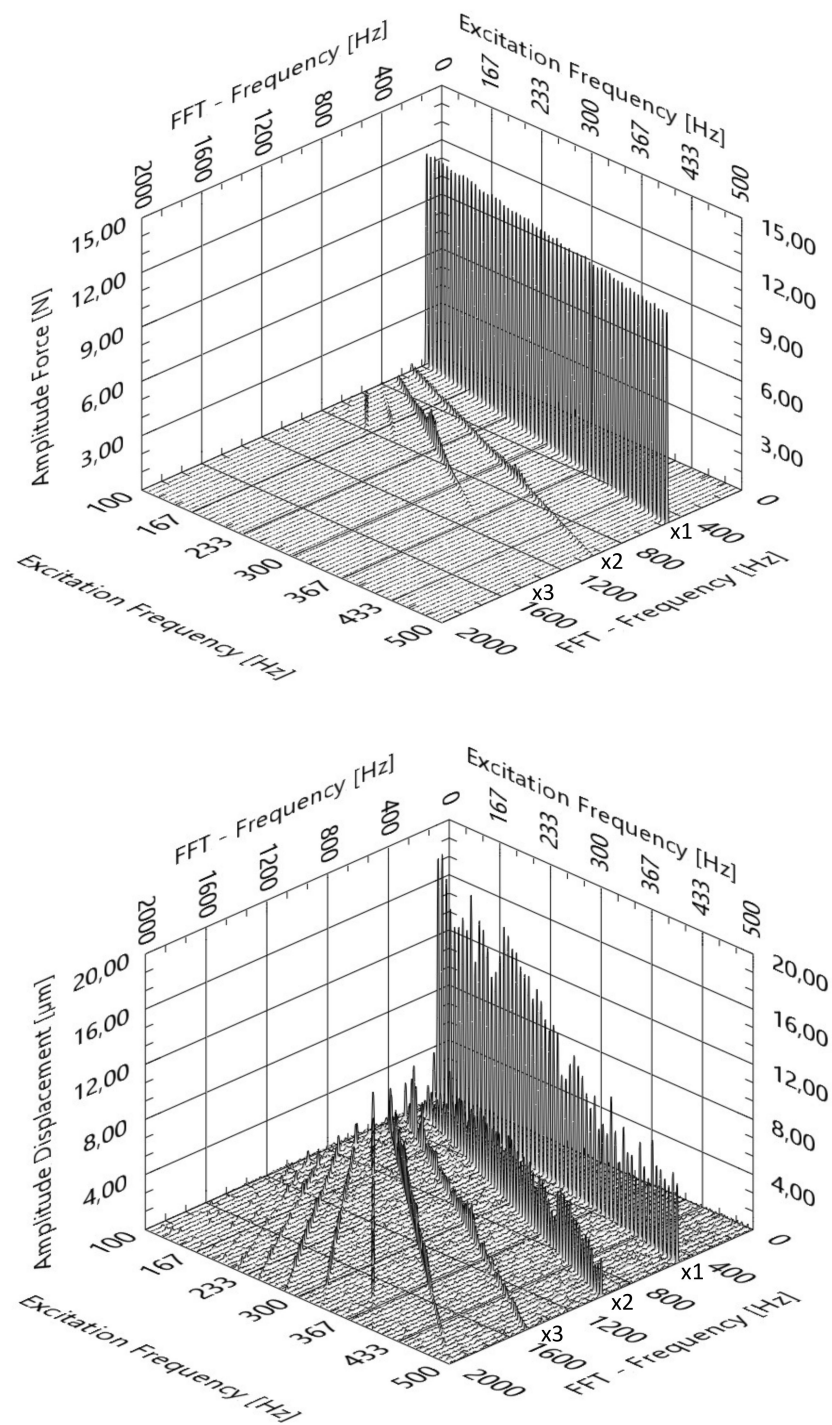
Figure A2. Waterfall plot of force and displacement sensor data in x-direction (11.1 N static load, 12 N force amplitude).
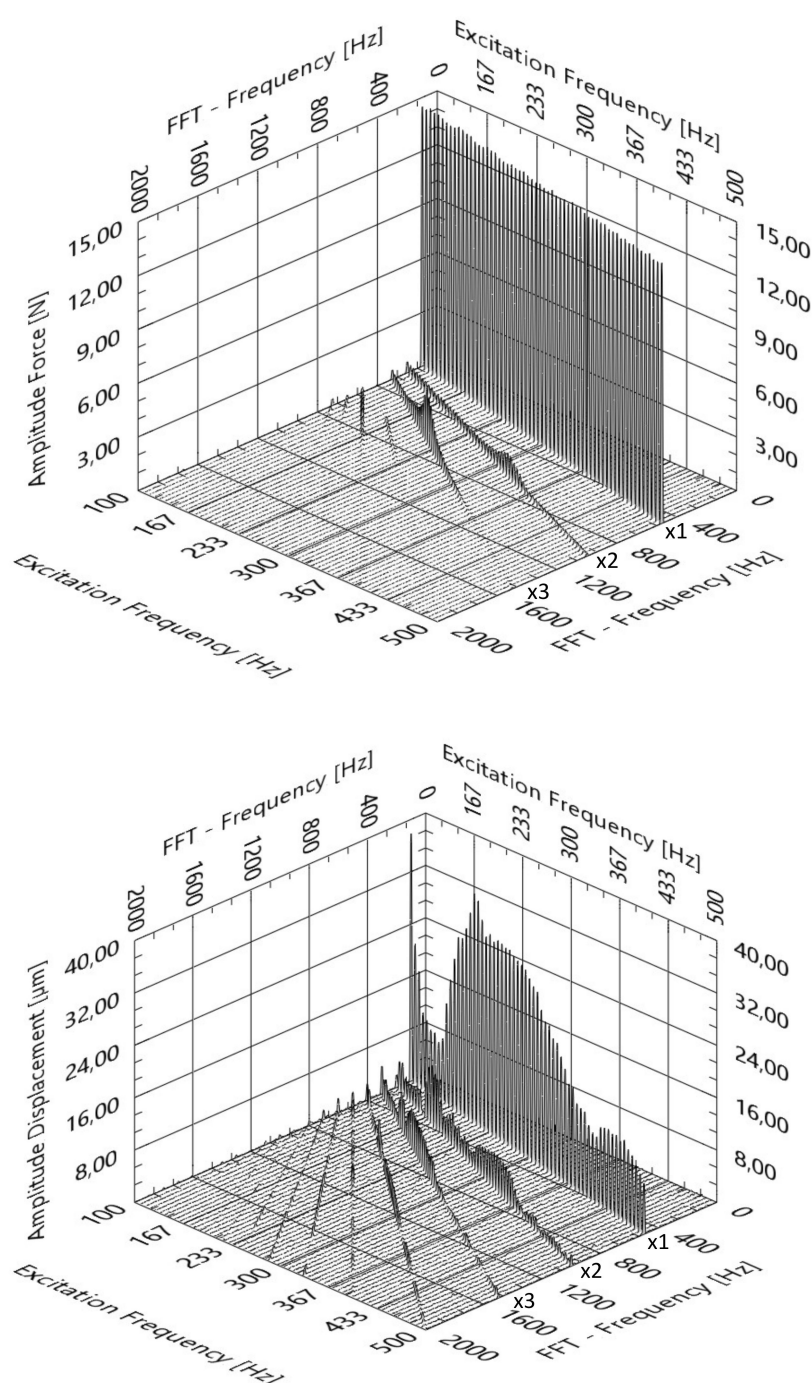
Figure A3. Waterfall plot of force and displacement sensor data in x-direction (11.1 N static load, 15 N force amplitude).

References

1. Performance of Simple Gas Foil Thrust Bearings in Air. Available online: https://ntrs.nasa.gov/search.jsp?R=20120003368 (accessed on 3 June 2020).
2. Agrawal, G.L. Foil Air/Gas Bearing Technology—An Overview. In *Proceedings of the ASME 1997 International Gas Turbine and Aeroengine Congress and Exhibition, Orlando, FA, USA, 2–5 June 1997*; American Society of Mechanical Engineers Digital Collection: Orlando, FL, USA, 1997; Volume 1.
3. Remaining Technical Challenges and Future Plans for Oil-Free Turbomachinery. Available online: https://ntrs.nasa.gov/archive/nasa/casi.ntrs.nasa.gov/20100033099.pdf (accessed on 27 March 2020).
4. Silver, A.; Marley, D.J. Selectively Pressurized Foil Bearing Arrangements. U.S. Patent US3366427A, 1 November 1965.

5. Heshmat, C.A.; Heshmat, H. An Analysis of Gas-Lubricated, Multileaf Foil Journal Bearings With Backing Springs. *J. Tribol.* **1995**, *117*, 437–443. [CrossRef]

6. Arakere, N.K. Analysis of foil journal bearings with backing springs. *Tribol. Trans.* **1996**, *39*, 208–214. [CrossRef]

7. Silver, A.; Wenban, J.R. Foil Bearing Stiffener. U.S. Patent US4153315A, 8 May 1979.

8. Du, J.; Zhu, J.; Li, B.; Liu, D. Hydrodynamic analysis of multileaf gas foil bearing with backing springs. *Proc. Inst. Mech. Eng. Part J J. Eng. Tribol.* **2014**, *228*, 529–547. [CrossRef]

9. Duan, W.; Sun, Y.; Geng, H.; Ding, C.; Yang, W.; Yu, L. Static performance of multi-leaf compliant Gas Foil Journal Bearings with assembly preload. In Proceedings of the 2013 IEEE International Conference on Mechatronics and Automation, Takamatsu, Japan, 4–7 August 2013; pp. 681–685.

10. Li, C.; Du, J.; Zhu, J.; Yao, Y. Effects of structural parameters on the load carrying capacity of the multi-leaf gas foil journal bearing based on contact mechanics. *Tribol. Int.* **2019**, *131*, 318–331. [CrossRef]

11. Childs, D.W.; Hale, K. A Test Apparatus and Facility to Identify the Rotordynamic Coefficients of High-Speed Hydrostatic Bearings. *J. Tribol.* **1994**, *116*, 337–343. [CrossRef]

12. San Andrés, L.; Chirathadam, T.A. Metal Mesh Foil Bearing: Effect of Motion Amplitude, Rotor Speed, Static Load, and Excitation Frequency on Force Coefficients. *J. Eng. Gas Turbines Power* **2011**, *133*, 122503. [CrossRef]

13. San Andrés, L.; De Santiago, O. Identification of Journal Bearing Force Coefficients under High Dynamic Loading Centered Static Operation. *Tribol. Trans.* **2005**, *48*, 9–17. [CrossRef]

14. Heshmat, H.; Ku, C.-P.R. Structural Damping of Self-Acting Compliant Foil Journal Bearings. *J. Tribol.* **1994**, *116*, 76–82. [CrossRef]

15. Rudloff, L.; Arghir, M.; Bonneau, O.; Matta, P. Experimental Analyses of a First Generation Foil Bearing: Startup Torque and Dynamic Coefficients. *J. Eng. Gas Turbines Power* **2011**, *133*, 092501. [CrossRef]

16. Delgado, A. Experimental Identification of Dynamic Force Coefficients for a 110 MM Compliantly Damped Hybrid Gas Bearing. *J. Eng. Gas Turbines Power* **2015**, *137*, 072502. [CrossRef]

17. Feng, K.; Liu, Y.; Zhao, X.; Liu, W. Experimental Evaluation of the Structure Characterization of a Novel Hybrid Bump-Metal Mesh Foil Bearing. *J. Tribol.* **2016**, *138*, 021702. [CrossRef]

18. Salehi, M.; Heshmat, H.; Walton, J.F. On the Frictional Damping Characterization of Compliant Bump Foils. *J. Tribol.* **2003**, *125*, 804–813. [CrossRef]

19. Kim, T.H.; Breedlove, A.W.; San Andrés, L. Characterization of a Foil Bearing Structure at Increasing Temperatures: Static Load and Dynamic Force Performance. *J. Tribol.* **2009**, *131*, 041703. [CrossRef]

20. Hoffmann, R. Eine Methode für Die Vorhersage Nichtlinearer Selbsterregter Schwingungen. Ph.D. Thesis, Technische Universität Berlin, Berlin, Germany, 27 February 2017.

21. Gloth, G.; Sinapius, M. Analysis of swept-sine runs during modal identification. *Mech. Syst. Signal Process.* **2004**, *18*, 1421–1441. [CrossRef]

22. Gloth, G.; Sinapius, M. Influence and characterisation of weak non-linearities in swept-sine modal testing. *Aerosp. Sci. Technol.* **2004**, *8*, 111–120. [CrossRef]

23. San Andrés, L.; Chirathadam, T.A.; Kim, T.-H. Measurement of Structural Stiffness and Damping Coefficients in a Metal Mesh Foil Bearing. *J. Eng. Gas Turbines Power* **2010**, *132*, 032503. [CrossRef]

24. DIN 40110-1. *Wechselstromgrößen; Zweileiter-Stromkreise*; DIN German Institute for Standardization, Beuth Verlag GmbH: Berlin, Germany, 1994.